SPECT Compton-Scattering Correction by Analysis of Energy Spectra

Kenneth F. Koral, Xiaoqin Wang, W. Leslie Rogers, Neal H. Clinthorne, and Xiaohan Wang

Division of Nuclear Medicine, University of Michigan, Ann Arbor, Michigan

The hypothesis that energy spectra at individual spatial locations in single photon emission computed tomographic projection images can be analyzed to separate the Compton-scattered component from the unscattered component is tested indirectly. An axially symmetric phantom consisting of a cylinder with a sphere is imaged with either the cylinder or the sphere containing ^{99m}Tc. An iterative peak-erosion algorithm and a fitting algorithm are given and employed to analyze the acquired spectra. Adequate separation into an unscattered component and a Compton-scattered component is judged on the basis of filtered-backprojection reconstruction of corrected projections. In the reconstructions, attenuation correction is based on the known geometry and the total attenuation cross section for water. An independent test of the accuracy of separation is not made. For both algorithms, reconstructed slices for the cold-sphere, hot-surround phantom have the correct shape as confirmed by simulation results that take into account the measured dependence of system resolution on depth. For the inverse phantom, a hot sphere in a cold surround, quantitative results with the fitting algorithm are accurate but with a particular number of iterations of the erosion algorithm are less good. (A greater number of iterations would improve the 26% error with the algorithm, however.) These preliminary results encourage us to believe that a method for correcting for Compton-scattering in a wide variety of objects can be found, thus helping to achieve quantitative SPECT.

J Nucl Med 29:195–202, 1988

For single photon emission computed tomography (SPECT) applications such as detecting cold liver lesions or quantifying tumor uptake, it is important to correct for counts from gamma rays that Compton scatter within the patient but still have sufficient energy so that their pulse height falls within the finite energy window of the tomograph. Lack of correction leads to low contrast images and uptake values that can depend on nearby structures.

Techniques for Compton-scatter correction have recently been reviewed (*1,2*). One interesting and quite practical method involves attempting to measure the scatter component for each projection element by collecting counts in a second, lower-energy (i.e., scatter) window adjacent to the primary full-energy (i.e., photopeak) window. The assumption is made that the image reconstructed from the scatter window can be multiplied by a parameter, k, and subtracted from the image reconstructed from the photopeak window to effect scatter correction (*3*). However, k may vary with the object being imaged and thus a single value of k may not apply to every imaging situation. Moreover, it hasn't been shown for any object that all parts of a tomogram are quantitatively accurate with a single k value.

It is the hypothesis of this work that complete energy spectra at individual spatial locations in each view can be analyzed to separate the Compton-scattering component from the unscattered component. To test the hypothesis, tomograms were reconstructed from Compton-corrected projection images. So that these tomograms can be judged quantitatively, an attenuation correction featuring a linear attenuation coefficient consistent with the total gamma-ray cross section is also employed. (In the future, this coefficient could be spatially dependent if that were warranted and the reconstruction algorithm made provision for it.)

Received Oct. 23, 1986; revision accepted July 8, 1987.

For reprints contact: Kenneth F. Koral, PhD, The University of Michigan, Division of Nuclear Medicine, R-3054 Kresge II, Ann Arbor, Michigan 48109-0021.

MATERIALS AND METHODS

Measurement and Analysis of Spatial Resolution

A measurement of system spatial resolution for a GE 400AT camera with a low-energy, general-purpose collimator was made to be used in simulating projection data. A thin capillary tube was filled with ^{99m}Tc and imaged at measured distances in front of the collimator ranging from 0 to 30 cm. A single 20% energy window was employed.

Resultant images were analyzed by drawing a wide profile perpendicular to the long axis of the capillary tube. The profiles were fit by a symmetric Gaussian function using the method of least squares. This method is suggested by the Nuclear Medicine Committee of the American Association of Physicists in Medicine when the data is acquired to a coarse grid (*4*) and has been used by other workers such as Macey et al. (*5*). The calculated full width at half maximum (FWHM) of the Gaussian was plotted versus depth. A straight line was fitted to these data, again by least squares.

Generation and Reconstruction of Simulated Data

In order to have ideal results to compare to experimental reconstructions, projection data were simulated for a nonradioactive (cold) sphere centrally located within a uniformly-radioactive (hot) cylinder. The center of the sphere was assumed to be on the axis of rotation 13.3 cm in front of the collimator, matching experimental conditions. For a slice through the center of the cold sphere, a 6-cm-diameter circle within a 21.5-cm-diameter circle was constructed on a fine grid within the computer. All elements at a given distance were then projected onto the camera ignoring attenuation and Compton-scattering. To simulate system resolution without scatter, this partial projection was then convoluted with a discretized Gaussian of the FWHM measured in air for the depth. The result was added into a total-projection array. After handling all the distances that had pixels containing activity, the projection image was complete.

Since the object is symmetric and we are interested in a noise-free result, this image can be replicated 32 times to form the projection-image set. Reconstruction is then carried out with a standard, filtered-backprojection program (MDS A^2 computer) with no attenuation correction. A medium-resolution filter is chosen. By reconstructing with bias on and again with bias off, one can see the negative values that are present in the reconstructed images and their profiles. One can also fix the true zero in profiles containing negatives.

Measurement of Experimental Data

The isotope employed was technetium-99m (^{99m}Tc) and the camera-collimator system was that mentioned previously. Acquisition mode was 64 × 64 word.

The phantom examined was axially symmetric—the 21.5 cm-diameter cylindrical Jaszczak phantom containing a centrally-located 6 cm-diameter sphere (Fig. 1). It was fitted with an adaption so it could be cantilevered over the top edge of the patient imaging table. In this way, there was no attenuation or scattering due to the table.

Spatially-dependent spectra were obtained in the following way: a very narrow (2-keV) window was set at the lowest energy of interest, 108 to 110 keV. An image of the object was acquired for a fixed time and stored. The window was then advanced to 110 to 112 keV and an acquisition obtained.

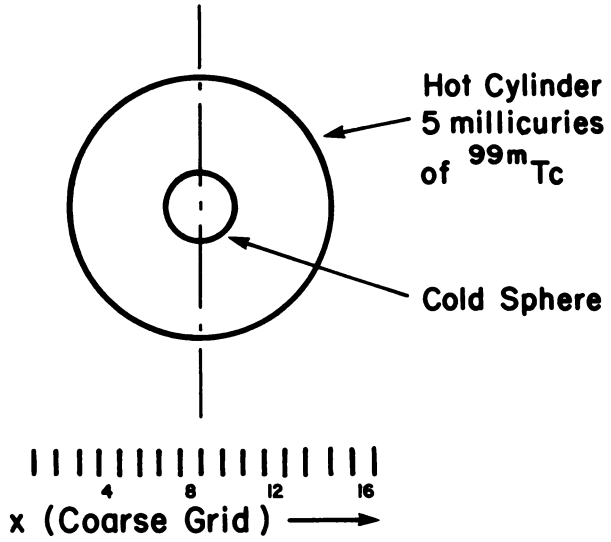

FIGURE 1
Sketch of slice through the symmetric phantom when the sphere is nonradioactive and the surround contains radioactivity. The y coordinate comes out of the page—a range of y values specifies the slice thickness. The x coordinate specifies location in the projection. For spectral analysis, x elements are grouped by four into the coarse grid shown.

This procedure was repeated 32 times in all. When the number of counts at any given position in the image is plotted versus energy the desired spectra is revealed.

The number of data sets was three.

1. A cold, water-filled sphere in a surround of radioactive water. No uniformity correction was applied but EAMP pulse-height correction was utilized. (This pulse-height correction is a part of the autotune feature of the camera. A camera-calibration procedure takes a set of energy spectra for different locations on the camera face under flood conditions and calculates and stores a correction factor for each—the EMAP. After that, energy signals during image acquisition are corrected so that spectral peaks occur at the same energy.)

2. A hot sphere (31.5 MBq) in a cold surround. Acquisition time for each 2-keV image in this case was 20 sec. In addition, a known-activity syringe in air was similarly imaged so that quantification of the hot sphere could be carried out using the syringe as a standard. No uniformity correction was applied but a new EMAP was acquired immediately before the data acquisitions.

3. A repeat of the cold sphere in a hot surround. At the same time, a syringe in air was imaged at five different locations to obtain a scatter-free spectra and check its variation with position. The syringe was placed at three different depths opposite the camera center and at a depth of 14 cm was displaced ±5 cm off center. Uniformity correction based on a 30 million-count flood was applied and an EMAP was again obtained immediately before the data acquisitions.

Analysis of Spectra

Data were transported to a MDS A^2 computer and also to The University of Michigan Amdahl computer. Spectra were obtained by placing 4 × 4 pixel (cold sphere) or a 4 × 16 pixel (hot sphere) regions of interest (x by y) on successive images.

The y value specifies the slice thickness. It was chosen to give a relatively thin slice through the center of the cold sphere yielding good contrast and to produce a thick slice covering the hot sphere so its activity could be quantified. The x value of 4 specifies that data are to be grouped to improve the statistical accuracy of points in the spectra.

The spectra are analyzed to obtain estimates of the spectra of Compton-scattering events. Then, after summation, a value for the total number of Compton-scatter counts at each location is obtained and used in correcting the projection image. The spectra are analyzed by two techniques.

1. The first is an interative peak erosion as described by East et al. (*6*). The result of successively reducing the peak height is an estimate of the Compton-scattering spectrum. The estimate depends on the number of iterations (i.e., "passes"). We did not use immediate updating of an element in the energy spectrum but otherwise followed the method as published. We employed four subsets (four plies in the terminology of East et al.).

2. The second is a fitting method which requires knowledge of the scatter-free spectra at the given spatial location. In this case, the shape of the Compton-scattering spectrum is assumed to be given by:

$$c_i = a_0 + a_1 i + a_2 i^2 + a_3 i^3, \quad (1)$$

where c_i is the number of counts in an energy bin, i is the bin number, and a_0, a_1, a_2, and a_3 are parameters to be determined from the fitting. The nonscattered spectrum, d_i, is assumed given in terms of the spectrum for the scatter-free source, f_i:

$$d_i = bf_i, \quad (2)$$

where b is another parameter to be found from the fitting. Then the total spectrum $\overline{y_i}$ is the sum of the scattered and unscattered components:

$$\overline{y_i} = c_i + d_i. \quad (3)$$

If the experimental spectrum is y_i, the parameters are found by getting the best fit between $\overline{y_i}$ and y_i. After the parameters are set, the Compton-scattering spectrum is given by Eq. (1).

The problem is written in standard least squares format and then solved by the method of Golub (*7*). Details are presented in Appendix A.

Calculation of Projection Image

For a given slice, spectrum analysis is carried out for each of the 16 spectra whose maximum exceeds a threshold percentage of the largest maximum for all x positions in the slice. After analysis, the Compton-scatter total is obtained by summing the scatter spectrum from channel n_1 (below the photopeak, typically at 117 keV) to channel n_2 (above the photopeak, typically at 162 keV). This Compton-scatter total is inserted into a scatter image at the appropriate x location. (Values of n_1 and n_2 were chosen by visual inspection.) A value of zero is inserted as scatter if the spectrum is not fit. An interpolative smoothing in x is then carried out (while maintaining counts) to obtain the 64 final scatter values.

The raw projection image of unscattered plus scattered gamma rays is formed by summing the raw data images over the same n_1 to n_2 range. Finally, a projection image corrected for Compton-scattering is estimated by subtraction of the scatter image from the raw image.

Attenuation Correction and Reconstruction

Since the phantom is composed of simple geometric shapes, the average transmission through it can be calculated as a function of distance along a diameter. The calculation utilizes the linear attenuation coefficient for ^{99m}Tc in water, 0.151 cm^{-1}. The Compton-corrected projection images are then further corrected for attenuation by dividing values by the appropriate transmission.

To prepare for reconstruction, the final projection image is replicated 32 times. Note that statistical inaccuracies can mimic nonuniformities in camera efficiency with this procedure, since they are not random with projection angle as they would be in an actual tomographic acquisition. Reconstruction of the image is carried out as it was for the simulated data.

Known-Activity Syringe

Processing of the known-activity syringe is a special case since it is assumed that Compton-scattering and attenuation had negligible effects. A slice width encompassing the syringe is chosen. No correction for Compton scattering is applied: the raw-data spectra are simply summed over the same n_1 to n_2 limits used for the hot sphere to produce the projection image. This image is replicated 32 times. No attenuation correction is applied before the reconstruction.

Scatter Fraction and Quantification

Once the spectrum at a given spatial location is separated into an unscattered and a Compton-scattered component, the scatter fraction, SF, can be calculated. We define this parameter as follows:

$$SF = \frac{S}{U}, \quad (4)$$

where S is total Compton-scattered counts and U is total unscattered counts. The total values are obtained from the respective spectra by summation. That is,

$$S = \sum_{i=n_1}^{n_2} c_i \quad (5)$$

$$U = \sum_{i=n_1}^{n_2} d_i \quad (6)$$

Quantification of the activity in the reconstructed hot sphere is obtained relative to the reconstructed, known-activity syringe. Regions of interest (ROIs) for the hot sphere and for the calibration syringe are determined in the respective slices by a commercial program which is based on spatial derivatives and starts from a hand-drawn first estimate. The activity in the sphere, A, is then calculated from the known activity in the syringe, A_s, by the proportionality

$$\frac{A}{A_s} = \frac{C}{C_s}, \quad (7)$$

where C is the number of counts in the sphere ROI and C_s is that in the syringe ROI. (The reconstruction scaling factors are also taken into account when evaluating the ratio of C to C_s.)

RESULTS

Spatial Resolution

The equation for the dependence of the full width at half maximum (FWHM) resolution, R, on distance in

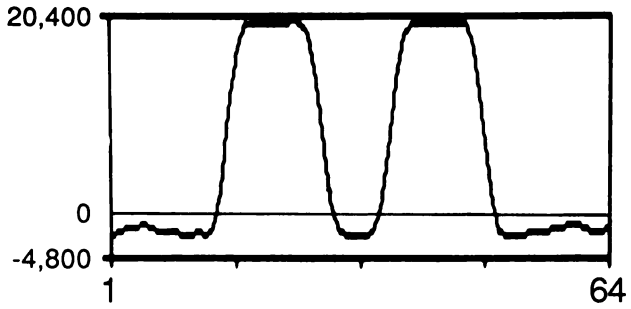

FIGURE 2
Reconstruction of simulated data for the cold-sphere, hot-surround phantom. No noise was added. Profile shown is through center of cold sphere. Negatives are included. Tomograms which are reconstructed from the experimental data can be compared with these ideal results.

front of the collimator, d, can be represented by

$$R = 6.35 \text{ mm} + 0.0467 * d. \quad (8)$$

This result is similar to that of a GE MaxiCamera II with a general purpose collimator (8). The MaxiCamera II is older than the 400 AT but they have comparable specifications for resolving alternating hot and cold bars, 3 and 2.5 mm, respectively.

Simulation

Simulated data for the cold-sphere phantom were reconstructed. A profile through the center of the sphere is shown in Figure 2. Experimental data will be compared with it.

First Cold-Sphere

The results of the erosion algorithm for a typical spectrum derived from the first set of experimental data for the cylindrical phantom containing a cold sphere are shown in Figure 3. It is seen that the end points in the estimate of the Compton-scattering spectrum are fixed but that the area under the curve decreases as the erosion algorithm proceeds from four to eight passes. The n_1 and n_2 limits for summation are shown.

The reconstruction for the data that has been corrected for attenuation and Compton-scattering is shown in Figure 4 at the right along with a profile through the center of the sphere. At left are the results for the data with attenuation correction but without the correction for Compton-scattering. It is seen that the image with Compton-correction is much more faithful to the true object.

Figure 5 compares the results when the Compton-scattering spectrum is estimated by four passes of the East et al. algorithm to those when it is estimated by eight. Negatives in the reconstructions are now shown whereas they were truncated in Figure 4. The four-pass result is very similar to the result with simulated data (Figure 2). Because of this similarity, we conclude four passes is optimum for this subject.

Hot Sphere

In the case of the hot sphere in a cold surround, both methods of estimating the Compton-scattering spectra were employed. Four passes of the East et al. algorithm were used since the results for the first cold sphere using four passes were judged superior to those using eight. The fitting algorithm employed a spectrum from the known-activity syringe to give the f_i in equation (*2*). An example of the data and the results from the fitting algorithm are shown in Figure 6.

The raw data for one projection of the hot sphere contained 35,269 counts so that the total counts for the thick slice are ~1,100,000 (32 × 35,269).

In Table 1, the calculated activity in the sphere for the two methods of estimating Compton scattering is given and is compared to the true activity. It is seen that the East et al. algorithm with four passes produces

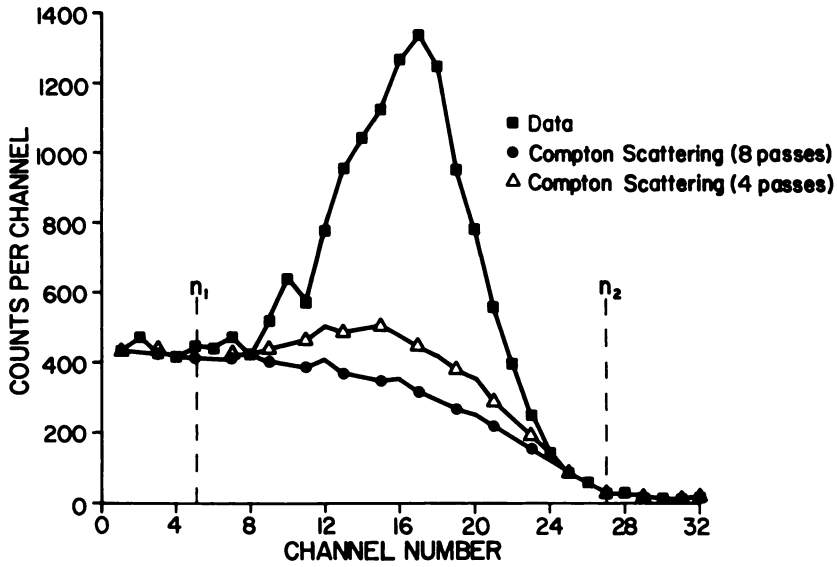

FIGURE 3
Plot of energy spectra for a typical x location for the case shown in Figure 1. The estimates of Compton scattering result from four and eight iterations of the erosion algorithm.

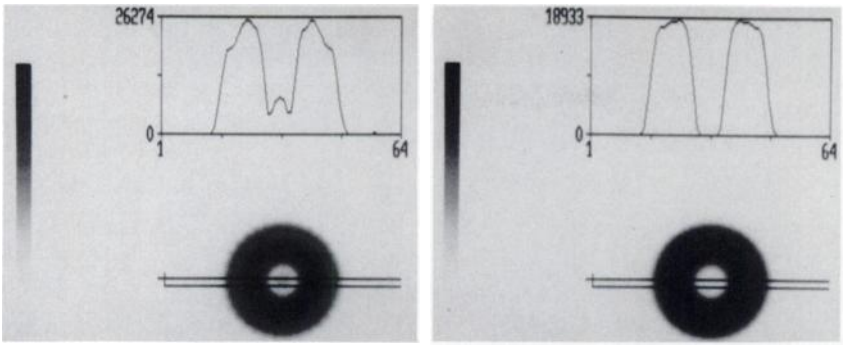

FIGURE 4
Cold sphere in a uniformly hot surround. Comparison of reconstruction results with (right) and without (left) four-pass Compton correction. Negatives in the images are set to zero. Without correction, there is an erroneous positive level at the location of the nonradioactive sphere and the high portions of the profile are not flat. With correction, the positive level disappears and the high portions approach being flat.

a value low by 26% but the fitting algorithm gives an exactly correct value.

Scatter-Free Spectra

The spectra for the syringe placed at different locations in front of the camera are shown in Figure 7. They are unnormalized—differences in area are presumably due to the decay of the radioisotope source and to any remaining nonuniformity in the camera sensitivity. It is seen that the spectra line up quite well and that any shape differences are slight. Therefore, in applying the fitting algorithm to the second set of data for the cold sphere in a hot cylinder, only a single spectrum was used to represent that of a scatter-free source: the one for the source opposite the center of the camera at a distance of 8 cm.

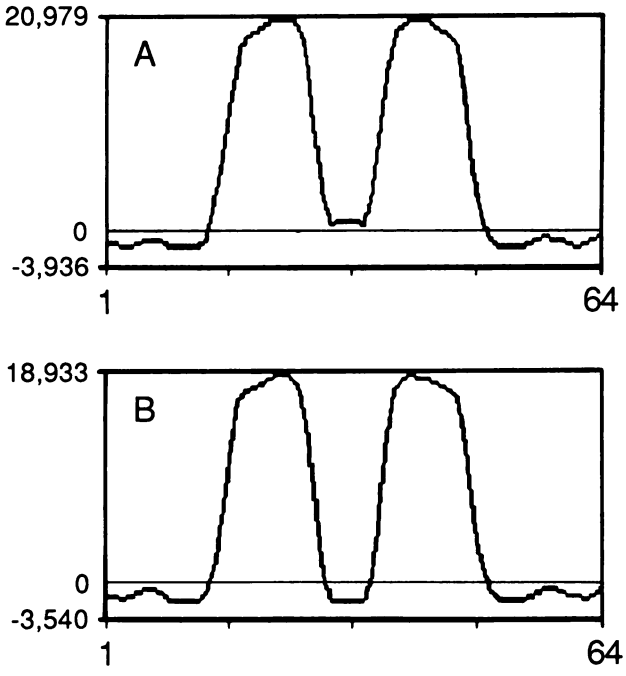

FIGURE 5
Effect of number of passes on reconstruction results for the same profile as in Figure 4 but with negative values shown. A: Eight passes, B: four passes.

Second Cold Sphere

For the second cold-sphere data set, the results of the reconstructions from the data with Compton scatter estimated by the fitting algorithm are as good as the better of the East et al. results for the first set of cold sphere data. The East et al. algorithm itself again produced good results but the slight variation in shape between four and eight passes wasn't observed.

Scatter Fraction

Table 2 shows the scatter fraction as a function of position as computed from the fitting results for both types of phantom. The results are given versus location number. Location 8 is nearest the centerline and location 1 is at the edge of the projection image. (Fig. 1). When no fitting of the spectrum was carried out, a dash is inserted. It is seen that the scatter fraction is large at the edge of both objects where direct events are falling rapidly but scattered events remain appreciable. For the hot cylinder with a cold sphere, the scatter fraction

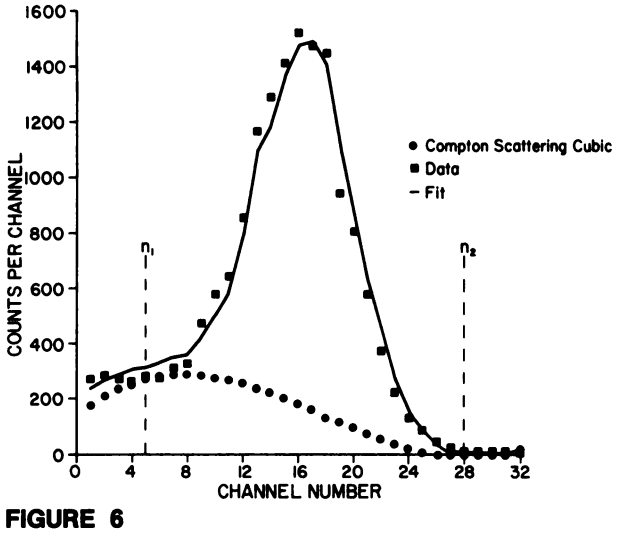

FIGURE 6
Plot of energy spectra for the cold cylindrical phantom containing a hot sphere. The fitting algorithm estimate for the Compton-scattering is shown at the bottom. The raw data and the fit to it are also shown. The x location number was eight on the coarse grid.

TABLE 1
Estimation of Sphere Activity*

Method of estimating Compton scattering	Calculated activity in sphere
East et al. four passes	23.3 MBq
Fitting	31.5 MBq

* True value = 31.5 MBq.

TABLE 2
Scatter Fraction as a Function of Location

Location number*	4	5	6	7	8
Cold sphere	0.746	0.367	0.477	0.534	0.668
Hot sphere	—	—	—	2.37	0.374

* 8.5 = centerline.

decreases sharply just inside the edge but then rises slowly as one progresses towards the center.

DISCUSSION

The first objective in this study was to show, at least indirectly, that the amount of Compton scattering within a specified energy window could be found as a function of spatial location within a tomographic projection image. We sought to do this in a preliminary way by examining two cases of a symmetric phantom—the sphere within a cylinder.

The method involved taking a complete energy spectrum at each of the spatial locations and operating on it with one or the other of two algorithms. The first, the technique of East et al., is a peak-erosion algorithm used in the analysis of complex gamma ray spectra obtained from many different gamma-ray sources. It has parameters to be specified and its final result is usually chosen to be that at a given pass number rather than that after a very large number of passes (i.e., iterations). It is inherently simple and is fast.

The second is a technique that involves fitting and requires knowledge of a scatter-free spectrum. It assumes that a cubic function will cover all of the spectral shapes for Compton scattering likely to be found in nuclear medicine applications.

The first objective of the study seems to have been realized in that the cold sphere in a hot surround was correctly reconstructed in a qualitative way by both algorithms. The hot sphere in a cold surround was also correctly reconstructed in a qualitative way and the fitting technique produced the correct quantitative value for total activity. This last result has great importance for the application of measuring tumor or critical-organ uptake so that radiation absorbed dose can be calculated in nuclear medicine therapies (*9–12*).

It should be noted, however, that the first objective was reached in an indirect way. That is, only final reconstructions were checked. Nowhere was it proved that the Compton-scattering spectrum or the sum for Compton-scattering with a specified window was correctly found.

The secondary objective was to distinguish between the two algorithms on the basis of accuracy. Here we did not fully meet the objective. The problem came from trying to optimize the number of passes in the erosion algorithm based on the cold-sphere phantom. The number of passes did produce a significant change in the number of counts subtracted from given pixels. However, this change had only a slight effect or no effect on the shape of the activity distribution, depending on the data set analyzed. So, the optimum number of passes was set at four but with a fair amount of uncertainty.

The fitting algorithm did surpass the four-pass ero-

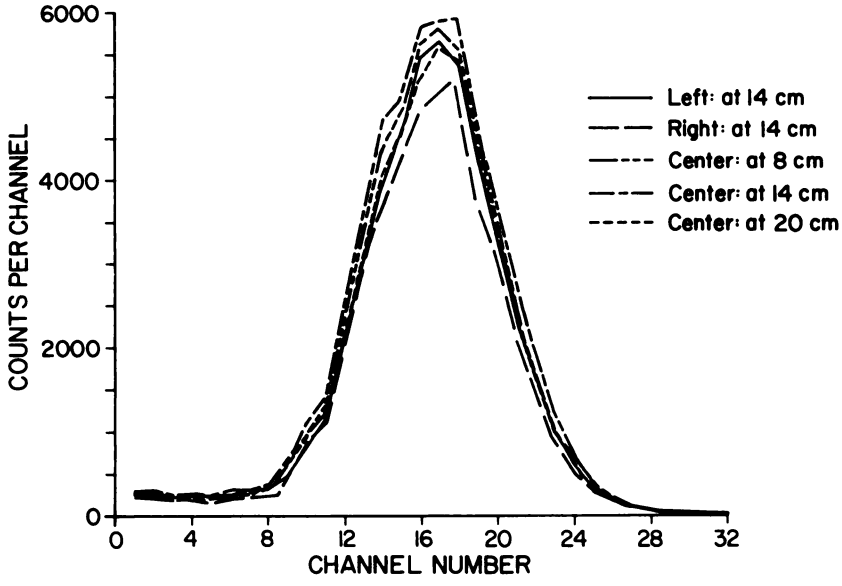

FIGURE 7
Energy spectra for a scatter-free source at a variety of locations. Shape differences were judged to be negligible.

sion algorithm in quantifying the hot sphere. However, four passes were used because of the desire to employ the same number of passes for the hot sphere as was thought optimum for the cold sphere. Actually, increasing the number of passes for the hot sphere would initially decrease the error. That is, a greater number of passes with erosion would increase the number of counts ascribed to unscattered gamma-rays, increase the calculated activity, and thus reduce the 26% error due to underestimating the activity.

The scatter fractions presented here could be compared to results of Monte Carlo simulations of Compton-scattering such as those of Floyd et al. (*13*), if similar objects were investigated by both methods. Our values are given for such a purpose. At present, however, a discrepancy could be explained by the neglect of the effects of the collimator in Monte Carlo simulations. Their Compton-scatter spectra for a line source in a large cylinder are similar to ours although somewhat more peaked.

In summary, more or different criterion may be needed to judge the quality of results of the two algorithms. Moreover, only if a Compton-scattering correction technique handles a large variety of geometries, will it have wide applicability. Therefore, both algorithms need to be applied to a variety of phantoms. Finally, relative behavior as the number of counts (i.e., the statistical noise level) is changed should also be assessed.

CONCLUSIONS

It has been shown that estimation of Compton scattering as a function of spatial location in a projection image is feasible.

A similar reconstruction for the inverse phantom, a hot sphere in a cold cylinder, has been shown to produce excellent quantitative results when the fitting algorithm is employed but less good results with 4 passes of the erosion algorithm.

APPENDIX A

Let the experimental spectrum to be fit be represented by y_i where i is an integer giving the bin number. By the previous assumptions, the fit results, $\bar{y}_i$, is the sum of scattered and unscattered components:

$$\bar{y}_i = c_i + d_i \tag{A1}$$

Now, let the channel numbers of interest for the fitting run from $i = n_1$ to $i = n_2$ and define some vectors:

$$\bar{Y} = \begin{pmatrix} \bar{y}_{n_1} \\ \bar{y}_{n_1+1} \\ \vdots \\ \vdots \\ n_2 \end{pmatrix} \quad Y = \begin{pmatrix} y_{n_1} \\ y_{n_1+1} \\ \vdots \\ y_{n_2} \end{pmatrix} \quad X = \begin{pmatrix} a_0 \\ a_1 \\ a_2 \\ a_3 \\ b \end{pmatrix} \tag{A2}$$

The first two have dimension M where $M = n_2 - n_1 + 1$ and the third has dimension 5.

The least squares problem is to minimize R with respect to the parameters a_0, a_1, a_2, a_3 and b where

$$R = \| \bar{Y} - Y \| \tag{A3}$$

and $\| \cdot \|$ denotes the 2-norm of a vector, i.e. the square root of the sum of the squares of its components.

Furthermore, from equations 1, 2, and A1 and using the bin range, we can write:

$$\bar{Y} = \underline{B}X = \begin{pmatrix} 1 & n_1 & n_1^2 & n_1^3 & f_{n_1} \\ 1 & n_1+1 & (n_1+1)^2 & (n_1+1)^3 & f_{n_1+1} \\ \cdot & \cdot & \cdot & \cdot & \cdot \\ \cdot & \cdot & \cdot & \cdot & \cdot \\ \cdot & \cdot & \cdot & \cdot & \cdot \\ 1 & n_2 & n_2^2 & n_2^3 & f_{n_2} \end{pmatrix} \begin{pmatrix} a_0 \\ a_1 \\ a_2 \\ a_3 \\ b \end{pmatrix} \tag{A4}$$

where $\underline{B}$ is a M × 5 Matrix.

In terms of B, R is given by

$$R = \| \underline{B}X - Y \| \tag{A5}$$

and can be solved by the method of Golub (*7*). On the Amdahl computer employing the Numerical Analysis and Applications Software (NAAS), the subroutine LLSQ is called and it returns the vextor X. The fitting is carried out with a weight equal to the inverse of the square root of y_i.

ACKNOWLEDGMENTS

This work was supported by PHS Grant Number CA38790 awarded by the National Cancer Institute, DHHS. The authors thank Jill Anderson for secretarial assistance in preparation of the manuscript.

REFERENCES

1. Jaszczak RJ, Floyd CE, Coleman RE. Scatter compensation techniques for SPECT. *IEEE Trans Nucl Sci* 1985; NS-32:786–793.
2. Oppenheim BE. Scatter correction for SPECT. *J Nucl Med* 1984; 25:928–929.
3. Jaszczak RJ, Greer KL, Floyd CE, et al. Improved SPECT quantification using compensation for scattered photons. *J Nucl Med* 1984; 25:893–900.
4. American Association of Physicists in Medicine Report No. 9. Computer-aided scintillation camera acceptance testing, 1981.
5. Macey DJ, DeNardo GL, DeNardo SJ, et al. Comparison of low- and medium-energy collimators for SPECT imaging with iodine-123-labeled antibodies. *J Nucl Med* 1986; 27:1467–1474.
6. East LV, Phillips RL, Strong AR. A fresh approach to NaI scintillation detector spectrum analysis. *Nucl Instrum Meth* 1982; 193:147–155.
7. Golub G. Numerical methods for solving linear least squares problems. *Numerische Math* 7, 206–216, 1965.
8. Hine GJ, Paras P, Warr CP, et al. Measurements of the performance parameters of gamma cameras: Part II. HEW Publications (FDA), 79-8049, June 1979.
9. Sisson JC, Shapiro B, Beierwaltes WH, et al. Radio-

pharmaceutical treatment of malignant pheochromocytomas. *J Nucl Med* 1984: 25:197–206.
10. Leichner PK, Klein JL, Siegelman SS, et al. Dosimetry of ^{131}I-labeled antiferritin in hepatoma: specific activities in tumor and liver. *Cancer Treat Rep* 1983; 67:647–658.
11. Hammond ND, Moldofsky PJ, Beardsley MR, et al. External imaging techniques for quantitation of distribution of I-131 $F(ab)_2$ fragments of monoclonal antibody in humans. *Med Phys* 1984; 11:778–783.
12. Koral KF, Meyers L, Botti J, et al. Correction of I-131 uptake-versus time curve obtained from conjugate views by an ^{123}I SPECT scan in a dosimetry application [Abstract]. *J Nucl Med* 1986; 27: 898–899.
13. Floyd CE, Jaszczak RJ, Harris CC, et al. Energy and spatial distribution of multiple order Compton scatter in SPECT: a Monte Carlo investigation. *Phys Med Biol* 1984; 29:1217–1230.